

# Application of the optimized-basis generator coordinate method to low-lying excited states of sd-shell nuclei

Moemi Matsumoto,<sup>1,\*</sup> Yusuke Tanimura,<sup>2</sup> and Kouichi Hagino<sup>3,4</sup>

<sup>1</sup>*Department of Physics, Tohoku University, Sendai, 980-8578, Japan*

<sup>2</sup>*Department of Physics and Origin of Matter and Evolution of Galaxies (OMEG) Institute, Soongsil University, Seoul 06978, Korea*

<sup>3</sup>*Department of Physics, Kyoto University, Kyoto, 606-8502, Japan*

<sup>4</sup>*RIKEN Nishina Center for Accelerator-based Science, RIKEN, Wako 351-0198, Japan*

(Dated: June 17, 2025)

We apply the optimized-basis generator coordinate method (OptGCM) to sd-shell nuclei,  $^{20}\text{Ne}$ ,  $^{24}\text{Mg}$ , and  $^{28}\text{Si}$ . This method variationally optimizes both the basis Slater determinants in the generator coordinate method (GCM) and the corresponding weight coefficients. To analyze the low-lying excited states of those nuclei, we implement the angular momentum projection. With the Skyrme interaction, we show that the simultaneous optimization of the basis functions and the weight factors lowers the energy of the excited states and at the same time leads to an appreciable effect on transition probabilities. These results highlight the effectiveness of the OptGCM method.

## I. INTRODUCTION

Collective motion is a characteristic feature of quantum many-body systems. In atomic nuclei, it has been known that various types of collective motions appear, such as the rotational motion of deformed nuclei and surface vibrations of spherical nuclei. The amplitude of those motions are often large, beyond the quadratic approximation around the ground state. Such large-amplitude collective motions play a crucial role in several phenomena in atomic nuclei, such as nuclear fission and shape coexistence.

To develop microscopic theories for collective motions is one of the central challenges in nuclear physics. Among such theories, the generator coordinate method (GCM) has been widely employed as a beyond-mean-field approach to large-amplitude collective motions [1–4]. In this method, a many-body state is constructed as a linear combination of configurations generated along specified collective coordinates, that characterize the essential degrees of freedom of the dynamics. The weight coefficients of the linear superposition are determined variationally. This method has been extensively used in nuclear structure theory, after implementing restoration of broken symmetries with the parity and the angular momentum projections[5–18].

A potential drawback of this method is that the selection of collective coordinates often relies on empirical knowledge. For instance, multipole moments of atomic nuclei have often been employed for such collective coordinates, but these may not be sufficient to accurately describe a given system. This problem represents a longstanding and significant challenge inherent to the method [1]. As a matter of fact, recent studies have demonstrated that the conventional empirical approaches to select collective coordinates may be insufficient to efficiently capture collective dynamics [19–21]. It is thus desirable to develop frameworks that do not rely on pre-fixed collective coordinates, in order not to miss essential degrees of

freedom. Towards this direction, a stochastic selection of the basis has been considered in Refs. [22–26]. Methods based on configuration interaction have also been proposed in Refs. [27–32].

Recently, we have developed a variational extension of the GCM (the optimized-basis GCM: OptGCM) that allows simultaneous optimization of both the single-particle states of the basis Slater determinants (SDs) and their corresponding weight coefficients [33]. See also Ref. [34] and Refs. [35, 36] for similar attempts in the frameworks of the Monte-Carlo shell model (MCSM) [34] and antisymmetrized molecular dynamics (AMD) [35, 36], respectively. In our previous work [33, 37], we applied the OptGCM to the intrinsic ground states of  $^{16}\text{O}$  and  $^{28}\text{Si}$ , and demonstrated that the basis optimization leads to a better description of the ground state of the systems.

In this paper, we extend our previous study and apply the OptGCM to study low-lying excited states of atomic nuclei [38]. To this end, we implement the angular momentum projection and compute spectra and transition probabilities of *sd*-shell nuclei.

The paper is organized as follows. In Sec. II, we detail the formalism of the OptGCM with angular momentum projection. In Sec. III, we apply the OptGCM to  $^{20}\text{Ne}$ ,  $^{24}\text{Mg}$ , and  $^{28}\text{Si}$  and discuss the role of basis optimization. We then summarize the paper in Sec. IV with future perspectives.

## II. METHOD

### A. Optimized-basis GCM (OptGCM)

In the GCM method, the trial wave function is expressed as

$$|\Psi\rangle = \sum_{a=1}^M f_a |\Phi_a\rangle, \quad (1)$$

where  $|\Phi_a\rangle$  are SDs constructed as antisymmetrized products of  $A$  orthonormal single-particle orbitals  $\varphi_i^{(a)}$  ( $i = 1, \dots, A$ ),  $A$  being the mass number of a nucleus. The total energy is

\* Current affiliation: Hitachi, Ltd., 1-280, Higashi-Koigakubo, Kokubunji-shi, Tokyo 185-8601, Japan

given by

$$E = \frac{\langle \Psi | H | \Psi \rangle}{\langle \Psi | \Psi \rangle} = \frac{\sum_{ab} f_a^* f_b H_{ab}}{\sum_{ab} f_a^* f_b N_{ab}}, \quad (2)$$

where  $N_{ab} = \langle \Phi_a | \Phi_b \rangle$  and  $H_{ab} = \langle \Phi_a | H | \Phi_b \rangle$  denote the norm and Hamiltonian kernels, respectively.

In the usual GCM, the energy is minimized with respect only to the weight coefficients  $f_a$  for a pre-fixed Slater determinants,  $|\Phi_a\rangle$ . In contrast, In the OptGCM, the total energy is minimized with respect both to the weight coefficients  $f_a$  and the single-particle orbitals  $\varphi_i^{(a)}$  [33]. That is, we impose the conditions of

$$\frac{\partial E}{\partial f_a^*} = 0, \quad (3)$$

and

$$\frac{\delta E}{\delta \varphi_i^{(a)*}} = 0. \quad (4)$$

Note that Eq. (3) yields the Hill-Wheeler equation, which is coupled to the equation for the single-particle wave functions, Eq. (4). We carry out the optimization with the conjugate gradient method [39], with initial SDs constructed with Woods-Saxon potentials with various quadrupole deformations. For the initial weight coefficients, we take  $f_a = 1$  for all  $a$ .

In this work, we adopt the SIII parameter set of the Skyrme energy density functional [40], and expand the single-particle wave functions on an axial harmonic oscillator basis [41] with 14 major shells. We impose axial and reflection symmetries, while we neglect the time-odd terms in the functional. The pairing correlations are also omitted for simplicity.

## B. Angular momentum projection

To directly compare theoretical results with experimental data, it is essential to restore rotational symmetry through the angular momentum projection. Ideally, the basis SDs in the OptGCM should be variationally optimized for each angular momentum  $I$ . Since this procedure is computationally demanding, we, as a first step, adopt a simplified approach, in which the basis SDs are optimized without the angular momentum projection. That is, we take the variation before the projection (VBP) for the angular momentum projection, rather than the variation after the projection (VAP). To this end, we first optimize the basis SDs  $|\Phi_a\rangle$  and the weight coefficients  $f_a$  for the intrinsic ground states, as described in the previous subsection. After the optimum set of the basis SDs are so obtained, we perform the angular momentum projection to restore the rotational symmetry and calculate low-lying excited states. That is, we apply the projection operator  $\hat{P}_{MK}^I$  onto Eq. (1) and obtain

$$|\Psi_{IM}\rangle = \sum_{a,K} f_{aK} \hat{P}_{MK}^I |\Phi_a\rangle. \quad (5)$$

Here,  $I$  is the total angular momentum and  $M$  and  $K$  are its projection onto the  $z$ -axis in the laboratory and the body-fixed frames, respectively. The weights are then re-determined by solving the Hill-Wheeler equation with the projected SDs for each angular momentum,  $I$ .

With the total wave function so obtained, we calculate the reduced electric transition probabilities,  $B(E2)$ . The  $B(E\lambda)$  for a transition between a state with spin  $I_i$  and that with  $I_f$  is given by [1]

$$B(E\lambda, I_i \rightarrow I_f) = \frac{1}{2I_i + 1} \left| \langle I_f | \hat{Q}_\lambda^{(e)} | I_i \rangle \right|^2, \quad (6)$$

where  $\langle I_f | \hat{Q}_\lambda^{(e)} | I_i \rangle$  is the reduced matrix element, and  $\hat{Q}_\lambda^{(e)}$  is the electric multipole operator given by

$$\hat{Q}_\lambda^{(e)} = e \int d\mathbf{r} \hat{\rho}_p(\mathbf{r}) r^\lambda Y_{\lambda\mu}(\hat{\mathbf{r}}). \quad (7)$$

Here,  $\hat{\rho}_p$  is the proton density operator and  $Y_{\lambda\mu}$  is the spherical harmonic.

For comparison, we also perform conventional GCM calculations with the quadrupole moment for the collective coordinate. In this approach, the basis SDs  $|\Phi(Q_2^{(a)})\rangle$  are local ground states obtained by the constrained Hartree-Fock (CHF) method with the constraint

$$\langle \Phi_a(Q_2^{(a)}) | \hat{Q}_2 | \Phi_a(Q_2^{(a)}) \rangle = Q_2^{(a)}. \quad (8)$$

Here,  $\hat{Q}_2$  is the quadrupole operator,

$$\hat{Q}_2 = \int d\mathbf{r} \hat{\rho}(\mathbf{r}) r^2 Y_{20}(\hat{\mathbf{r}}), \quad (9)$$

where  $\hat{\rho}$  and  $Y_{20}$  are the density operator and the spherical harmonic, respectively. As in the OptGCM, the weights are determined after the angular momentum projection is performed.

## III. RESULTS AND DISCUSSIONS

### A. Intrinsic ground states

Let us now apply the OptGCM to the  $^{20}\text{Ne}$ ,  $^{24}\text{Mg}$ , and  $^{28}\text{Si}$  nuclei. For  $^{20}\text{Ne}$  and  $^{28}\text{Si}$ , we superpose 10 SDs, while we superpose 8 SDs for  $^{24}\text{Mg}$  in both OptGCM and GCM calculations. We have confirmed that the results are not significantly changed even if we increase the number of SDs.

We first discuss the intrinsic ground state. Table I summarizes the energies of the intrinsic ground state of  $^{20}\text{Ne}$ ,  $^{24}\text{Mg}$ , and  $^{28}\text{Si}$  obtained with the Hartree-Fock (HF), the GCM, and the OptGCM calculations. In the case of  $^{20}\text{Ne}$ , the energy decreases by 0.56 MeV from HF to GCM, and it further decreases by 0.87 MeV from GCM to OptGCM. Similarly, for  $^{24}\text{Mg}$  ( $^{28}\text{Si}$ ), the energy decreases by 0.74 (1.19) MeV from HF to GCM, and by 0.91 (0.78) MeV from GCM to OptGCM. These are consistent with the results of our previous study presented in Ref. [33].

To understand the energy gains due to the basis optimization in OptGCM, Figure 1 shows several quantities obtained

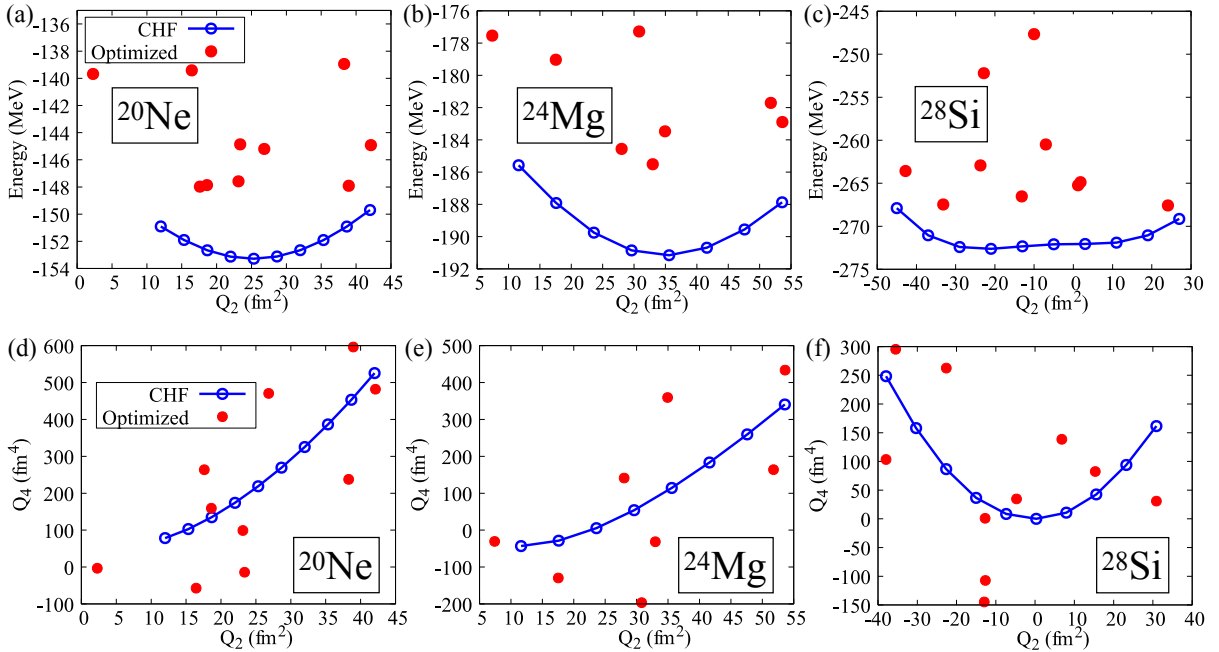


FIG. 1. The upper row: the energy expectation values of the basis SDs obtained with the CHF (the blue circles) and the OptGCM (the red dots) for (a)  $^{20}\text{Ne}$ , (b)  $^{24}\text{Mg}$ , and (c)  $^{28}\text{Si}$  nuclei. These are plotted as a function of the expectation values of the quadrupole moments  $Q_2$ . The lower row: the quadrupole and the hexadecapole moments,  $Q_2$  and  $Q_4$ , of the basis SDs obtained with the CHF (the blue circles) and the OptGCM (the red dots) for (d)  $^{20}\text{Ne}$ , (e)  $^{24}\text{Mg}$ , and (f)  $^{28}\text{Si}$  nuclei.

TABLE I. The energies (in MeV) of the intrinsic ground states of  $^{20}\text{Ne}$ ,  $^{24}\text{Mg}$ , and  $^{28}\text{Si}$  obtained with the HF, GCM, and OptGCM calculations.

	HF	GCM	OptGCM
$^{20}\text{Ne}$	-153.28	-153.84	-154.71
$^{24}\text{Mg}$	-191.21	-191.95	-192.86
$^{28}\text{Si}$	-228.74	-229.93	-230.71

with the optimized basis states for the intrinsic ground state. Figures 1 (a), (b), and (c) present the expectation value of the energy for each basis state as a function of  $Q_2$  for the  $^{20}\text{Ne}$ ,  $^{24}\text{Mg}$ , and  $^{28}\text{Si}$  nuclei, respectively. The blue lines represent the potential energy curves (PECs) obtained using CHF calculations. Since we do not take into account the pairing correlation in the present calculations, the CHF calculations for  $^{20}\text{Ne}$  and  $^{24}\text{Mg}$  do not converge around  $Q_2 = 0$  due to level crossings. We exclude those points in the PEC.

In all the three nuclei studied in this paper, the optimized basis states lie upper than each of the PECs, thus correspond to excited states for a given value of  $Q_2$ . This is similar to our previous result for  $^{16}\text{O}$  [33]. Despite the large diagonal elements of the Hamiltonian in the optimized basis, the ground-state energies obtained with OptGCM are still lower than those with the conventional GCM. This energy gain arises from the enhanced off-diagonal matrix elements in the optimized basis [37]. These results indicate that taking a superposition of solely the local ground states does not necessarily

lead to a good ground state. The OptGCM incorporates many-body correlations in a more complex way than the conventional GCM.

Figures 1 (d), (e), and (f) present scatter plots of the quadrupole moment  $Q_2$  and hexadecapole moment  $Q_4$ , calculated for each basis state in  $^{20}\text{Ne}$ ,  $^{24}\text{Mg}$ , and  $^{28}\text{Si}$ , respectively. The red dots represent the results with the OptGCM basis states, while the blue circles correspond to those obtained from the CHF calculations with constraint on  $Q_2$ . While the local ground states obtained with CHF trace the valley of the potential energy surface, the OptGCM results exhibit considerable fluctuations around the valley. This behavior indicates that collective dynamics of  $Q_4$  as well as  $Q_2$  are efficiently taken into account in the OptGCM states. These results suggest that, at least for the nuclei considered in this study, it is necessary to include higher-order multipole moments, at least up to  $Q_4$ , in the collective coordinates in order to optimize the intrinsic ground states. Furthermore, we point out that the OptGCM is also advantageous from a computational perspective, as it reduces the technical efforts required to perform multidimensional GCM calculations, which would require many mesh points in a multi-dimensional potential energy surface.

## B. Low-lying states with angular momentum projection

We next discuss the results for excited states. Figures 2 (a), (b), and (c) show the calculated and experimental ground-state

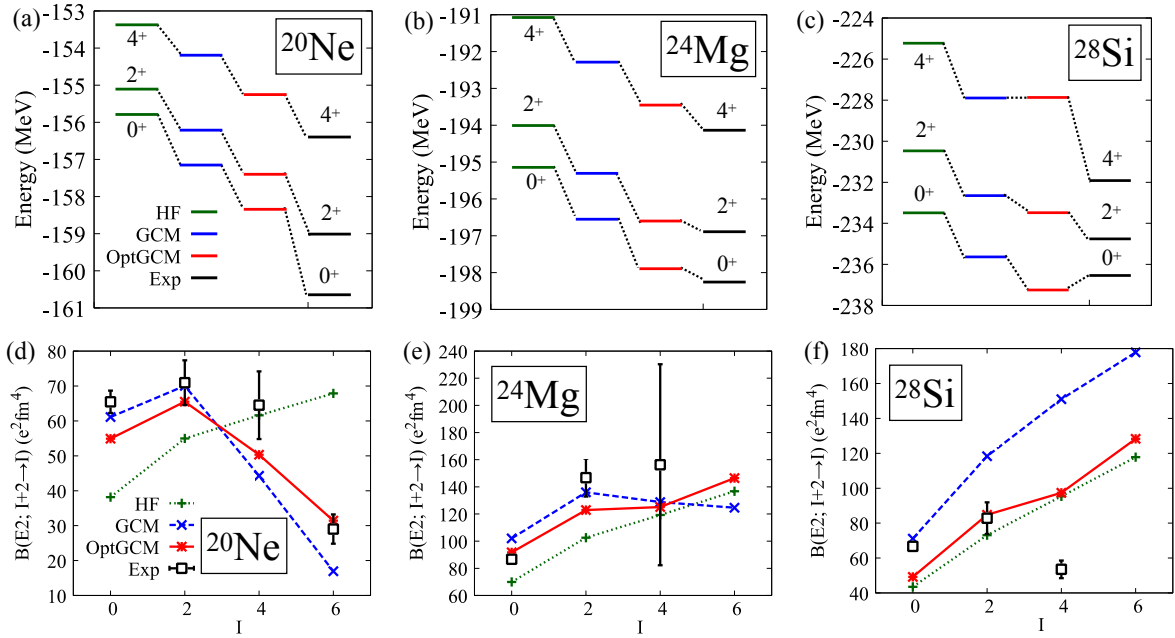


FIG. 2. The energy spectra for the (a)  $^{20}\text{Ne}$ , (b)  $^{24}\text{Mg}$ , and (c)  $^{28}\text{Si}$  nuclei obtained with the HF, the GCM, and the OptGCM with the angular momentum projection, in comparison with the experimental data. Comparisons of the calculated  $B(E2)$  values with the experimental data are also shown in the lower panels. The experimental data are taken from Ref. [42].

rotational spectra of the  $^{20}\text{Ne}$ ,  $^{24}\text{Mg}$ , and  $^{28}\text{Si}$  nuclei, respectively, obtained with the HF, the GCM, and the OptGCM calculations. The experimental data are taken from Ref. [42]. One can see that the energies of the  $0^+$ ,  $2^+$ , and  $4^+$  states decrease successively from the HF to the GCM and further to the OptGCM, similar to the intrinsic states shown in Table I. Therefore, for these low-lying states, the OptGCM results represent an improvement over both the HF and the standard GCM. Notice that the decrease of the ground-state energies after the angular momentum projection is comparable to that for the intrinsic states.

As the angular momentum increases, the differences in energy between the OptGCM and the GCM become smaller. This is the case particularly for the  $4^+$  state in  $^{28}\text{Si}$ . A part of the reason for this is that the basis states of the OptGCM in these calculations are optimized with respect to the intrinsic ground states and it is unreasonable to assume that such basis states can efficiently describe excited states with large excitation energies. This limitation would be removed by optimizing basis states for each angular momentum individually. We also note that the OptGCM yields the ground state energy of  $^{28}\text{Si}$  that is lower than the experimental value. This, however, would not be a serious problem given that the SIII parameter set of the Skyrme interaction is designed for HF calculations, rather than beyond-mean-field calculations such as those with the GCM and the OptGCM. Even with such interaction, one would still be able to discuss differences of the results among the models.

Figures 2 (d), (e), and (f) present the  $B(E2)$  transition strengths for the  $^{20}\text{Ne}$ ,  $^{24}\text{Mg}$ , and  $^{28}\text{Si}$  nuclei. For all the

three nuclei, both the GCM and the OptGCM lead to a reasonably good agreement with the experimental data, except for  $B(E2 : 6^+ \rightarrow 4^+)$  in  $^{28}\text{Si}$ . In particular, in the case of  $^{20}\text{Ne}$ , the angular momentum dependence of  $B(E2)$  is well described both with the GCM and the OptGCM, whereas the HF leads to an inconsistent angular momentum dependence. The reduction in  $B(E2)$  at  $I = 2$  is known as the effect of band termination, signaling the end of the ground-state rotational band [43]. Table II compares the  $B(E2)$  values of  $^{20}\text{Ne}$  obtained in our calculations (the OptGCM, the GCM, and the HF) with the results of other theoretical approaches, such as the relativistic Hartree-Bogoliubov (RHB) [44], the relativistic Hartree plus BCS (RH+BCS) [45], and the antisymmetrized molecular dynamics (AMD) [46], as well as with the experimental data [42]. The results of the OptGCM and the GCM are consistent with those of the other beyond-mean-field methods and show good agreement with the experimental data. We mention that those beyond-mean-field methods do not impose reflection symmetry, in contrast to our calculations. However, the potential energy surfaces of  $^{20}\text{Ne}$  reported in Refs. [44, 45] suggest that the impact of reflection symmetry breaking is negligible.

#### IV. SUMMARY AND FUTURE PERSPECTIVES

We have investigated the low-lying states of the  $^{20}\text{Ne}$ ,  $^{24}\text{Mg}$ , and  $^{28}\text{Si}$  nuclei using the OptGCM developed in our previous work [33]. In contrast to the previous work, we have implemented the angular momentum projection in the Opt-

TABLE II. The observed (Exp.) and the calculated (OptGCM, GCM, and HF) intraband  $E2$  transition probabilities  $B(E2; I_i^\pi \rightarrow I_f^\pi)$ , in units of  $e^2 \text{fm}^4$ , within the  $K^\pi = 0_1^+$  band for  $^{20}\text{Ne}$ . These are compared with the results of the relativistic Hartree-Bogoliubov (RHB) with DD-PC1 interaction [44], the relativistic Hartree+BCS (RH+BCS) with PC-PK1 interaction [45], the deformed-basis AMD with Gogny D1S interaction [46], and the  $(sd)^4$  shell model (SM) [47].

$I_i^\pi \rightarrow I_f^\pi$	Exp.	OptGCM	GCM	HF	RHB	RH+BCS	AMD	SM
$2^+ \rightarrow 0^+$	$65 \pm 3$	54.9	61.1	38.1	54	74	70.3	57
$4^+ \rightarrow 2^+$	$71 \pm 6$	65.5	70	55	89	71	83.7	69.9
$6^+ \rightarrow 4^+$	$64 \pm 10$	50.3	44.3	61.6	85	68	52.7	57.9
$8^+ \rightarrow 6^+$	$29 \pm 4$	31.4	16.9	67.9			21	35.5

GCM to compute a spectrum and transition probabilities. To reduce a computational cost, we have first optimized the basis states for the intrinsic ground state and then performed the angular momentum projection. We have compared the results with those obtained by the HF, the conventional GCM, and the available experimental data. Comparisons were also made with a few previous theoretical studies.

Although some variations specific to each nucleus were observed, we have observed several common features. First, the OptGCM consistently yields lower energies for the low-lying states compared to the HF and the GCM. According to the variational principle, a lower energy implies a closer approximation to the exact solution for a given many-body Hamiltonian. This indicates that the OptGCM leads to an improvement over the HF and the GCM, at least for the nuclei studied in this paper. Second, an analysis of the energies and multipole moments of the basis SDs suggests that nontrivial many-body correlations are incorporated into the OptGCM wave function as a result of the basis optimization.

The present method can be further extended in several ways. This includes optimizing the basis states for each angular momentum, as has been done in MCSM [34]. This will improve the description of excited states. An extension of the framework to include the pairing correlation by replacing the SDs by Hartree-Fock-Bogoliubov (HFB) states is also an important future work, particularly for describing open-shell nuclei as well as nuclear deformation. Furthermore, remov-

ing the constraints of axial and reflection symmetry will allow a description of more general nuclear shapes. Systematic applications to a variety of nuclei, along with comparisons with other theoretical approaches such as the conventional GCM, the self-consistent collective coordinate (SCC) method [48–51], and the dynamical GCM with collective momenta [19, 20, 52], will also help to identify the relevant collective degrees of freedom.

Another interesting future direction is to extend the current method to time-dependent frameworks in order to describe nuclear dynamics, such as fusion and fission processes. Preliminary calculations using the AMD basis have suggested that a description of many-body quantum tunneling [36] will be possible with such an extension. In this context, it is worth noting that several research groups have recently developed time-dependent extensions of the GCM framework [53–56].

#### ACKNOWLEDGMENTS

This work was supported by JST SPRING grant No. JP-MJSP2114, and the JSPS KAKENHI grants No. 19K03861, 23K03414, and 24KJ0352. M. M. acknowledges the support from the Graduate Program on Physics for the Universe (GP-PU) of Tohoku University. Y. T. acknowledges support from the Basic Science Research Program of the National Research Foundation of Korea (NRF) under grants No. RS-2024-00361003, RS-2024-00460031, and RS- 2021-NR060129.

---

[1] P. Ring and P. Schuck, *The Nuclear Many-Body Problem* (Springer Verlag Berlin-Heidelberg, 1980).

[2] M. Bender, P.-H. Heenen, and P.-G. Reinhard, Self-consistent mean-field models for nuclear structure, *Rev. Mod. Phys.* **75**, 121 (2003).

[3] T. Nikšić, D. Vretenar, and P. Ring, Relativistic nuclear energy density functionals: Mean-field and beyond, *Prog. Part. Nucl. Phys.* **66**, 519 (2011).

[4] W. Younes, D. M. Gogny, and J.-F. Berger, *A Microscopic Theory of Fission Dynamics Based on the Generator Coordinate Method*, (Springer Nature Switzerland AG, 2019).

[5] J. M. Yao, M. Bender, and P.-H. Heenen, Systematics of low-lying states of even-even nuclei in the neutron-deficient lead region from a beyond-mean-field calculation, *Phys. Rev. C* **87**, 034322 (2013).

[6] Y. Fu, H. Mei, J. Xiang, Z. P. Li, J. M. Yao, and J. Meng, Beyond relativistic mean-field studies of low-lying states in neutron-deficient krypton isotopes, *Phys. Rev. C* **87**, 054305 (2013).

[7] J. M. Yao, E. F. Zhou, and Z. P. Li, Beyond relativistic mean-field approach for nuclear octupole excitations, *Phys. Rev. C* **92**, 041304 (2015).

[8] J. M. Yao, L. S. Song, K. Hagino, P. Ring, and J. Meng, Systematic study of nuclear matrix elements in neutrinoless double- $\beta$  decay with a beyond-mean-field covariant density functional theory, *Phys. Rev. C* **91**, 024316 (2015).

[9] M. Bender and P.-H. Heenen, Beyond mean-field description of the low-lying spectrum of  $^{16}\text{O}$ , *Nuclear Physics A* **713**, 390 (2003).

[10] M. Bender, H. Flocard, and P. H. Heenen, Beyond-mean-field-model analysis of low-spin normal-deformed and superde-

formed collective states of  $^{32}\text{S}$ ,  $^{36}\text{Ar}$ ,  $^{38}\text{Ar}$ , and  $^{40}\text{Ca}$ , *Phys. Rev. C* **68**, 044321 (2003).

[11] B. Bally, B. Avez, M. Bender, and P.-H. Heenen, Beyond mean-field calculations for odd-mass nuclei, *Phys. Rev. Lett.* **113**, 162501 (2014).

[12] T. Duguet, M. Bender, P. Bonche, and P.-H. Heenen, Shape coexistence in  $^{186}\text{Pb}$ : beyond-mean-field description by configuration mixing of symmetry restored wave functions, *Physics Letters B* **559**, 201 (2003).

[13] T. R. Rodríguez and J. Luis Egido, A beyond mean field analysis of the shape transition in the Neodymium isotopes, *Physics Letters B* **663**, 49 (2008).

[14] R. Rodríguez-Guzmán, J. Egido, and L. Robledo, Correlations beyond the mean field in magnesium isotopes: angular momentum projection and configuration mixing, *Nuclear Physics A* **709**, 201 (2002).

[15] R. R. Rodríguez-Guzmán, J. L. Egido, and L. M. Robledo, Beyond mean field description of shape coexistence in neutron-deficient Pb isotopes, *Phys. Rev. C* **69**, 054319 (2004).

[16] T. R. Rodríguez and J. L. Egido, New Beyond-Mean-Field Theories: Examination of the Potential Shell Closures at  $N = 32$  or 34, *Phys. Rev. Lett.* **99**, 062501 (2007).

[17] L. M. Robledo, T. R. Rodríguez, and R. R. Rodríguez-Guzmán, Mean field and beyond description of nuclear structure with the gogny force: a review, *Journal of Physics G: Nuclear and Particle Physics* **46**, 013001 (2018).

[18] R. Rodríguez-Guzmán, L. M. Robledo, and P. Sarriguren, Microscopic description of quadrupole-octupole coupling in Sm and Gd isotopes with the Gogny energy density functional, *Phys. Rev. C* **86**, 034336 (2012).

[19] N. Hizawa, K. Hagino, and K. Yoshida, Generator coordinate method with a conjugate momentum: Application to particle number projection, *Phys. Rev. C* **103**, 034313 (2021).

[20] N. Hizawa, K. Hagino, and K. Yoshida, Applications of the dynamical generator coordinate method to quadrupole excitations, *Phys. Rev. C* **105**, 064302 (2022).

[21] C. V. N. Kumar and L. M. Robledo, Hexadecapole axial collectivity in the rare earth region: A beyond-mean-field study, *Phys. Rev. C* **108**, 034312 (2023).

[22] N. Itagaki, A. Kobayakawa, and S. Aoyama, New description of light nuclei by extending the AMD approach, *Phys. Rev. C* **68**, 054302 (2003).

[23] P. Descouvemont and N. Itagaki,  $^9\text{Be}$  scattering with microscopic wave functions and the continuum-discretized coupled-channel method, *Phys. Rev. C* **97**, 014612 (2018).

[24] P. Descouvemont and N. Itagaki, A stochastic microscopic approach to the  $^{10}\text{Be}$  and  $^{11}\text{Be}$  nuclei, *Prog. Theor. Exp. Phys.* **2020**, 023D02 (2020).

[25] S. Shinohara, H. Ohta, T. Nakatsukasa, and K. Yabana, Configuration mixing calculation for complete low-lying spectra with a mean-field Hamiltonian, *Phys. Rev. C* **74**, 054315 (2006).

[26] Y. Fukuoka, S. Shinohara, Y. Funaki, T. Nakatsukasa, and K. Yabana, Deformation and cluster structures in  $^{12}\text{C}$  studied with configuration mixing using Skyrme interactions, *Phys. Rev. C* **88**, 014321 (2013).

[27] A. Faessler and A. Plastino, Multi-configuration Hartree-Fock theory in nuclei, *Z. Phys. A* **220**, 88 (1969).

[28] L. Satpathy and Q. Ho-Kim, Multiconfiguration Field Theory in Nuclei, *Phys. Rev. Lett.* **25**, 123 (1970).

[29] L. Satpathy and Q. Ho-Kim, Multiconfiguration Field Theory in Nuclei [Erratum], *Phys. Rev. Lett.* **25**, 782 (1970).

[30] N. Pillet, C. Robin, M. Dupuis, G. Hupin, and J. F. Berger, The self-consistent multiparticle-multiparticle configuration mixing, *Eur. Phys. J. A* **53** (2017).

[31] C. Robin, N. Pillet, D. Peña Arteaga, and J.-F. Berger, Description of nuclear systems with a self-consistent configuration-mixing approach: Theory, algorithm, and application to the  $^{12}\text{C}$  test nucleus, *Phys. Rev. C* **93**, 024302 (2016).

[32] C. Robin, N. Pillet, M. Dupuis, J. Le Bloas, D. Peña Arteaga, and J.-F. Berger, Description of nuclear systems with a self-consistent configuration-mixing approach. II. Application to structure and reactions in even-even  $sd$ -shell nuclei, *Phys. Rev. C* **95**, 044315 (2017).

[33] M. Matsumoto, Y. Tanimura, and K. Hagino, Extension of the generator coordinate method with basis optimization, *Phys. Rev. C* **108**, L051302 (2023).

[34] N. Shimizu, T. Abe, Y. Tsunoda, Y. Utsuno, T. Yoshida, T. Mizusaki, M. Honma, and T. Otsuka, New-generation Monte Carlo shell model for the K computer era, *Prog. Theor. Exp. Phys.* **2012** (2012), 01A205.

[35] T. Myo, M. Lyu, Q. Zhao, M. Isaka, N. Wan, H. Takemoto, and H. Horiuchi, Variation of multi-slater determinants in antisymmetrized molecular dynamics and its application to  $^{10}\text{Be}$  with various clustering, *Phys. Rev. C* **108**, 064314 (2023).

[36] N. Hasegawa, K. Hagino, and Y. Tanimura, Time-dependent generator coordinate method for many-particle tunneling, *Phys. Lett. B* **808**, 135693 (2020).

[37] M. Matsumoto, Y. Tanimura, and K. Hagino, Non-empirical description of nuclear collective motion with optimized basis for multi-reference density functional theory, *EPJ Web Conf.* **306**, 01040 (2024).

[38] M. Matsumoto, Y. Tanimura, and K. Hagino, Generator coordinate method with basis optimization, *Acta Phys. Pol. B Proc. Suppl.* **18**, 2 (2025).

[39] W. H. Press, S. A. Teukolsky, W. T. Vetterling, and B. P. Flannery, *Numerical Recipes in Fortran 77*, Vol. 1 *Fortran Numerical Recipes* (Cambridge University Press, 1986).

[40] M. Beiner, H. Flocard, N. Van Giai, and P. Quentin, Nuclear ground-state properties and self-consistent calculations with the Skyrme interaction: (I). Spherical description, *Nucl. Phys. A* **238**, 29 (1975).

[41] D. Vautherin, Hartree-Fock Calculations with Skyrme's Interaction. II. Axially Deformed Nuclei, *Phys. Rev. C* **7**, 296 (1973).

[42] D. Tilley, C. Cheves, J. Kelley, S. Raman, and H. Weller, Energy levels of light nuclei,  $a = 20$ , *Nuclear Physics A* **636**, 249 (1998).

[43] A. Afanasjev, D. Fossan, G. Lane, and I. Ragnarsson, Termination of rotational bands: disappearance of quantum many-body collectivity, *Physics Reports* **322**, 1 (1999).

[44] P. Marević, J.-P. Ebran, E. Khan, T. Nikšić, and D. Vretenar, Quadrupole and octupole collectivity and cluster structures in neon isotopes, *Phys. Rev. C* **97**, 024334 (2018).

[45] E. Zhou, J. Yao, Z. Li, J. Meng, and P. Ring, Anatomy of molecular structures in  $^{20}\text{Ne}$ , *Phys. Lett. B* **753**, 227 (2016).

[46] M. Kimura, Deformed-basis antisymmetrized molecular dynamics and its application to  $^{20}\text{Ne}$ , *Phys. Rev. C* **69**, 044319 (2004).

[47] T. Tomoda and A. Arima, Coexistence of shell structure and cluster structure in  $^{20}\text{Ne}$ , *Nucl. Phys. A* **303**, 217 (1978).

[48] T. Marumori, T. Maskawa, F. Sakata, and A. Kuriyama, Self-Consistent Collective-Coordinate Method for the Large-Amplitude Nuclear Collective Motion, *Prog. Theor. Phys.* **64**, 1294 (1980).

[49] M. Matsuo, Treatment of Nucleon-Number Conservation in the Selfconsistent Collective-Coordinate Method: —Coupling between Large-Amplitude Collective Motion and Pairing Rotation—, *Prog. Theor. Phys.* **76**, 372 (1986).

[50] M. Matsuo, T. Nakatsukasa, and K. Matsuyanagi, Adiabatic Selfconsistent Collective Coordinate Method for Large Amplitude Collective Motion in Nuclei with Pairing Correlations, *Prog. Theor. Phys.* **103**, 959 (2000).

[51] N. Hinohara, T. Nakatsukasa, M. Matsuo, and K. Matsuyanagi, Microscopic Derivation of Collective Hamiltonian by Means of the Adiabatic Self-Consistent Collective Coordinate Method: Shape Mixing in Low-Lying States of  $^{68}\text{Se}$  and  $^{72}\text{Kr}$ , *Prog. Theor. Phys.* **119**, 59 (2008).

[52] K. Goeke and P.-G. Reinhard, The generator-coordinate-method with conjugate parameters and the unification of microscopic theories for large amplitude collective motion, *Annals of Physics* **124**, 249 (1980).

[53] B. Li, D. Vretenar, T. Nikšić, P. W. Zhao, and J. Meng, Generalized time-dependent generator coordinate method for small- and large-amplitude collective motion, *Phys. Rev. C* **108**, 014321 (2023).

[54] B. Li, D. Vretenar, T. Nikšić, P. W. Zhao, and J. Meng, Generalized time-dependent generator coordinate method for induced fission dynamics, *Front. Phys.* **19**, 44201 (2024).

[55] B. Li, D. Vretenar, T. Nikšić, P. W. Zhao, and J. Meng, Microscopic model for yields and total kinetic energy in nuclear fission, *Phys. Rev. C* **111**, L051302 (2025).

[56] P. Marević, D. Regnier, and D. Lacroix, Multiconfigurational time-dependent density functional theory for atomic nuclei: technical and numerical aspects, *Eur. Phys. J. A* **60** (2024).